Earth Planets Space, **61**, 299–318, 2009

Coseismic displacements and slip distribution from GPS and leveling observations for the 2006 Peinan earthquake (M_w 6.1) in southeastern Taiwan

Horng-Yue Chen[1], Ya-Ju Hsu[1], Jian-Cheng Lee[1], Shui-Beih Yu[1], Long-Chen Kuo[1], Yen-Lin Jiang[1], Chi-Ching Liu[1], and Chun-Shyong Tsai[2]

[1]*Institute of Earth Sciences, Academia Sinica, 128, Sec. 2, Academia Road, Nankang, Taipei, Taiwan, 115*
[2]*Seismological Center, Central Weather Bureau, Taiwan*

(Received August 16, 2007; Revised May 16, 2008; Accepted October 27, 2008; Online published March 3, 2009)

Since 2001, we have set up a dense geodetic network with 52 campaign-mode GPS sites and seven continuously recording GPS stations as well as six leveling routes in the Taitung area, Taiwan. Our aim was to better characterize near-fault crustal deformation of active faults at the plate suture of the Philippine Sea plate and Eurasia in southeastern Taiwan. On 1 April 2006, a moderate shallow earthquake (M_w 6.1, depth 10.8 km) occurred within this network. This earthquake resulted from rupturing of a geologically unknown or suspected fault (called the Y fault) located underneath the eastern margin of the Central Range. After removing the impacts of secular motions and postseismic slip, we estimated the coseismic displacements of the Peinan earthquake from the GPS and leveling measurements before and after the main shock. Three deformation types with distinct slip behaviors were revealed in three different regions: (1) near the epicenter—around 45 mm movement in the S-SSW direction with +20 to −20 mm vertical motion, in the northern part of the Y fault; (2) south of the epicenter across the southern part of the Y fault—approximately 35 mm in a westward movement with −60 mm subsidence (footwall side) and 40 mm in a SSW movement with at least 50 mm uplift (hanging-wall side), in the southern part of the Y fault; (3) northeast away from the epicenter—about 10 mm in a northward displacement with +15 to −10 mm vertical motions, in the Longitudinal Valley and on the western flank of the Coastal Range. This unique coseismic deformation pattern sheds new light on the characteristics of the suture zone between the Eurasian and Philippine Sea plates at the southernmost Longitudinal Valley. We used GPS and leveling measurements to invert for the fault geometry and the coseismic slip distribution. The optimal modeled fault is an 80° west-dipping fault at a depth of 0.5–20 km. The highest slip of about 0.33 m is located to the south of the hypocenter at a depth of 9–16 km. The total geodetic moment in our optimal model is 2.3×10^{18} Nt-m, which is equivalent to an earthquake of M_w 6.2. The surface coseismic displacements as well as the inferred coseismic slip distribution indicate a drastic change of slip behaviors in the middle of the Y fault. The left-lateral slippage near the hypocenter turned dramatically to reverse faulting with left-lateral component as rupturing propagated to the southern portion of the fault, suggesting that a possible right-lateral faulting occurred that coseismically cross cut the northern middle Peinanshan massif in the Longitudinal Valley.

Key words: GPS, precise leveling, coseismic deformation, slip distribution, peinan earthquake, Taiwan.

1. Introduction

The 150-km-long Longitudinal Valley represents the plate suture of the active collision between the Eurasian and Philippine Sea plates in eastern Taiwan (Fig. 1(a)). During the past decades, scientists have carried out a variety of quantitative and qualitative analyses to better understand the processes of the plate suture zone in this arc-continent collision (Hsu, 1962; Barrier *et al*., 1982; Ho, 1986; Yu and Liu, 1989; Yu *et al*., 1992; Lee and Angelier, 1993; Angelier *et al*., 1997; Lee *et al*., 1998; Hu *et al*., 2001; Yu and Kuo, 2001; Shyu *et al*., 2008). Efforts from previous studies indicated a rapid shortening of about 30 mm/year in the middle and southern segments of the Longitudinal Valley Fault (LVF), which is the major fault of the plate suture in the valley (Yu *et al*., 1992; Yu and Kuo, 2001; Lee *et al*., 2003). However, a more complex architecture of the fault system and tectonic context with at least two branches (i.e., the Luyeh fault to the west and the Lichi fault to the east) and a few secondary strike-slip faults have been reported in the southern end of the LVF (Fig. 1(b)) (Yu *et al*., 1992; Lee *et al*., 1998; Hu *et al*., 2001; Yu and Kuo, 2001). A possible major west-dipping back-thrust was also suspected to be developing at the eastern edge of the Central Range of the Eurasian plate to the west of the valley (Biq, 1965; Shyu *et al*., 2007), complicating the LVF fault system at the plate suture.

In an attempt to better characterize crustal deformation, fault structures, and fault behaviors of the southernmost Longitudinal Valley, since 2001 we have been conducting a multi-year project of repeated geodetic measurements, including GPS as well as the precise leveling surveys. We have also been integrating data of continuously

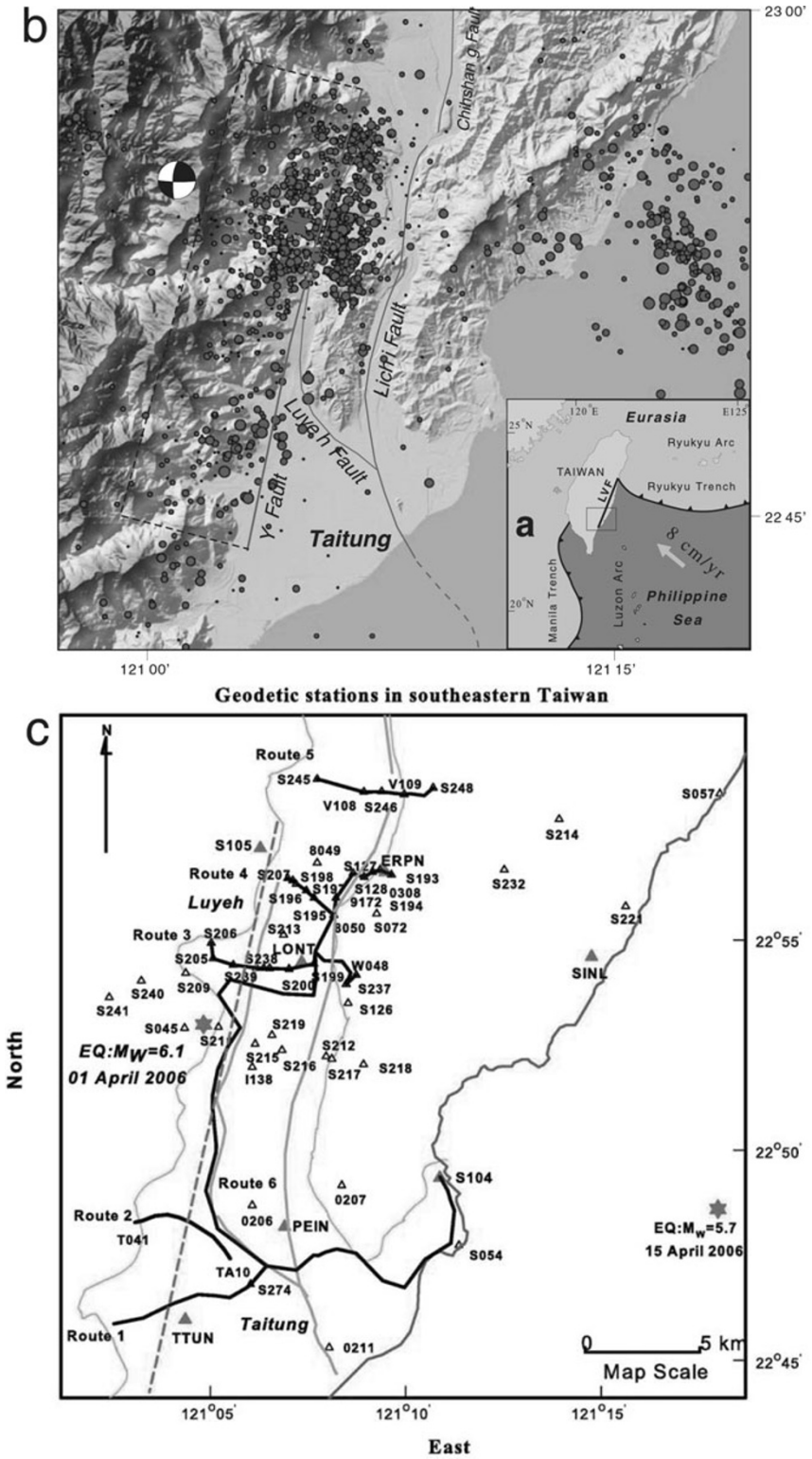

Fig. 1. (a) Tectonic framework of the Taiwan area. The Longitudinal Valley Fault (LVF) represents the plate suture between the Eurasian and Philippine Sea plates. (b) Distribution of the main shock (red star) and the aftershocks of the 2006 M_w 6.1 Peinan earthquake. The major geological faults, including the Chihshang fault, the Lichi fault, the Luyeh fault, and the blind Y fault, are shown in the 40-m DEM topographic shading map. The rectangle with dash lines represents the presumable fault plane of the deeply west-dipping Y fault. (c) Geodetic sites in southeastern Taiwan. The solid triangle presents the continuous GPS stations (CGPS). The open triangle represents the campaign GPS sites (CMS). The numbered solid lines denote the precise leveling routes.

recording GPS stations from a continuous GPS network in Taiwan (CORS), installed by the Institute of Earth Sciences, Academia Sinica (IES) and Central Weather Bureau (CWB), together with data from 52 campaign-mode sites (CMS) that were installed by IES in 2001 (Fig. 1(c)). In addition, six leveling routes E-W across the valley and N-S along the valley were also deployed and have been surveyed annually since 2001. These geodetic networks provide a

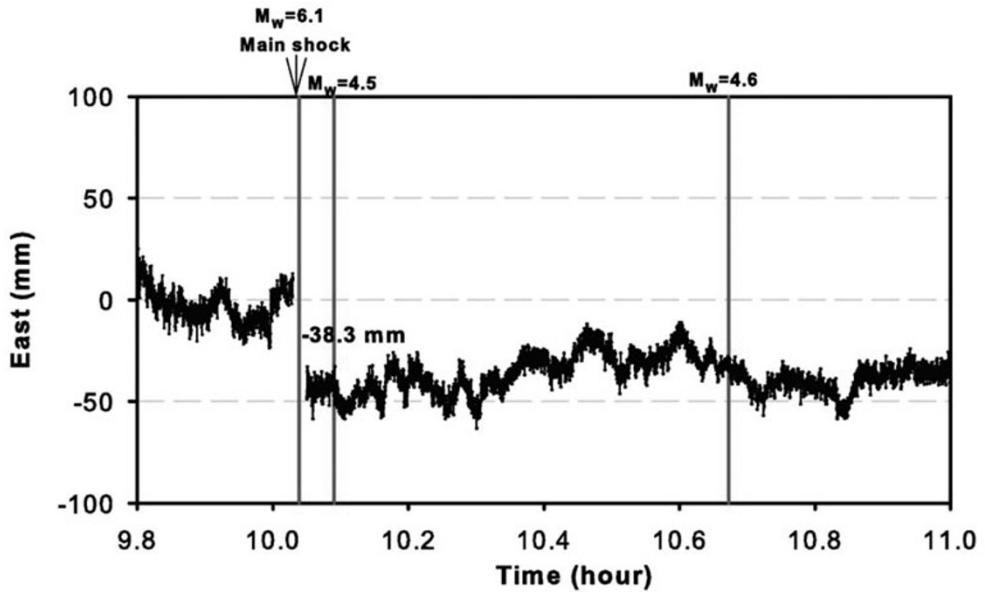

Fig. 2. Single epoch solution in 1 Hz sampling rate at station PEIN, which is a CGPS site close to the main shock. The east component shows significant coseismic displacement. There are no obvious displacements associated with the two following major aftershocks of M_L 4.6 and 4.8.

rather good spatial coverage for studying the fault activity of the southern Longitudinal Valley in great detail.

The M_w 6.1 Peinan earthquake struck the Taitung County in southeast Taiwan on 1 April 2006 (Fig. 1(b)). This moderate earthquake, which occurred within this geodetic network, provides an opportunity to carry out a more detailed characterization of the seismogenic structures in the southern Longitudinal Valley.

The aim of the study reported here was to illustrate detailed surface deformation associated with the Peinan earthquake using GPS observations and leveling measurements (Fig. 1). The observed horizontal and vertical coseismic displacements were used to determine the causative fault(s) and to analyze the fault motion during the earthquake. We used an elastic dislocation model to invert the coseismic fault geometry and slip distribution. Based on our results, we propose a kinematic model of faulting for the 2006 Peinan earthquake.

2. The 2006 Peinan Earthquake

The 2006 M_w 6.1 Peinan earthquake (M_L 6.4) occurred at the southern end of the Longitudinal Valley in eastern Taiwan (Fig. 1(b)) with a focal depth of about 10 km (Wu *et al.*, 2006). The main shock induced strong ground shaking in the surrounding villages and in the vicinity of Taitung City, the largest city in southeastern Taiwan (110,000 habitants). Numerous aftershocks occurred; these were centered mainly around the main shock along the eastern margin of the Central Range and underneath the Longitudinal Valley (Fig. 1(b)). In addition, the largest aftershock, with magnitudes of up to 5.7, was triggered 14 days after the main shock at a location 25 km east of the epicenter (Fig. 1(b)). This cluster of aftershocks was interpreted to result from reactivation of the main LVF system, which is different from the causative fault of the main shock, according to the locations and earthquake focal mechanisms of the aftershocks (Wu *et al.*, 2006).

The focal mechanism of the main shock indicates a strike-slip faulting (Fig. 1(b)). However, two immediate major aftershocks ($M_w = 4.5$ and 4.6) of reverse faulting occurred 3 and 28 min after the main shocks. We examined the available 1-Hz GPS data from a continuous GPS (CGPS) station (PEIN; Fig. 2). The data showed that the station recorded a clear coseismic displacement of the main shock, especially in the E-W component (about 38 mm, with respect to the station in the stable continental margin). On the other hand, no significant surface displacement can be observed following two aftershocks. Note that this -38.3 mm of coseismic displacement is slightly different than the -34.1 mm obtained from the daily solution (Fig. 3), a subject that will be discussed in more detail in the next section. Hence, we interpret that the coseismic displacements estimated from the daily solutions of continuous GPS stations to be mainly attributed to the main shock. In addition, we observed significant postseismic surface deformation at some of CGPS stations in a time span of few weeks to few months, which we will discuss in the later section.

The Peinan earthquake was interpreted to result from a rupture of a NNE-trending fault, which is located underneath the eastern margin of the Central Range, according to the focal mechanism of the main shock and the distribution of aftershocks (Wu *et al.*, 2006). This is a geologically poorly known fault, although several scientists have suspected its existence based on various measurements (Biq, 1965; Lu and Malavieille, 1994; Shyu *et al.*, 2007). As a result, we name this coseismic rupture as the Y fault. The Peinan earthquake indeed provides an opportunity to better examine the nature of the Y fault.

3. GPS Data Acquisition and Processing

In order to estimate the surface coseismic displacement associated with the 2006 Peinan earthquake, we included not only the CGPS data from the CORS network but also the

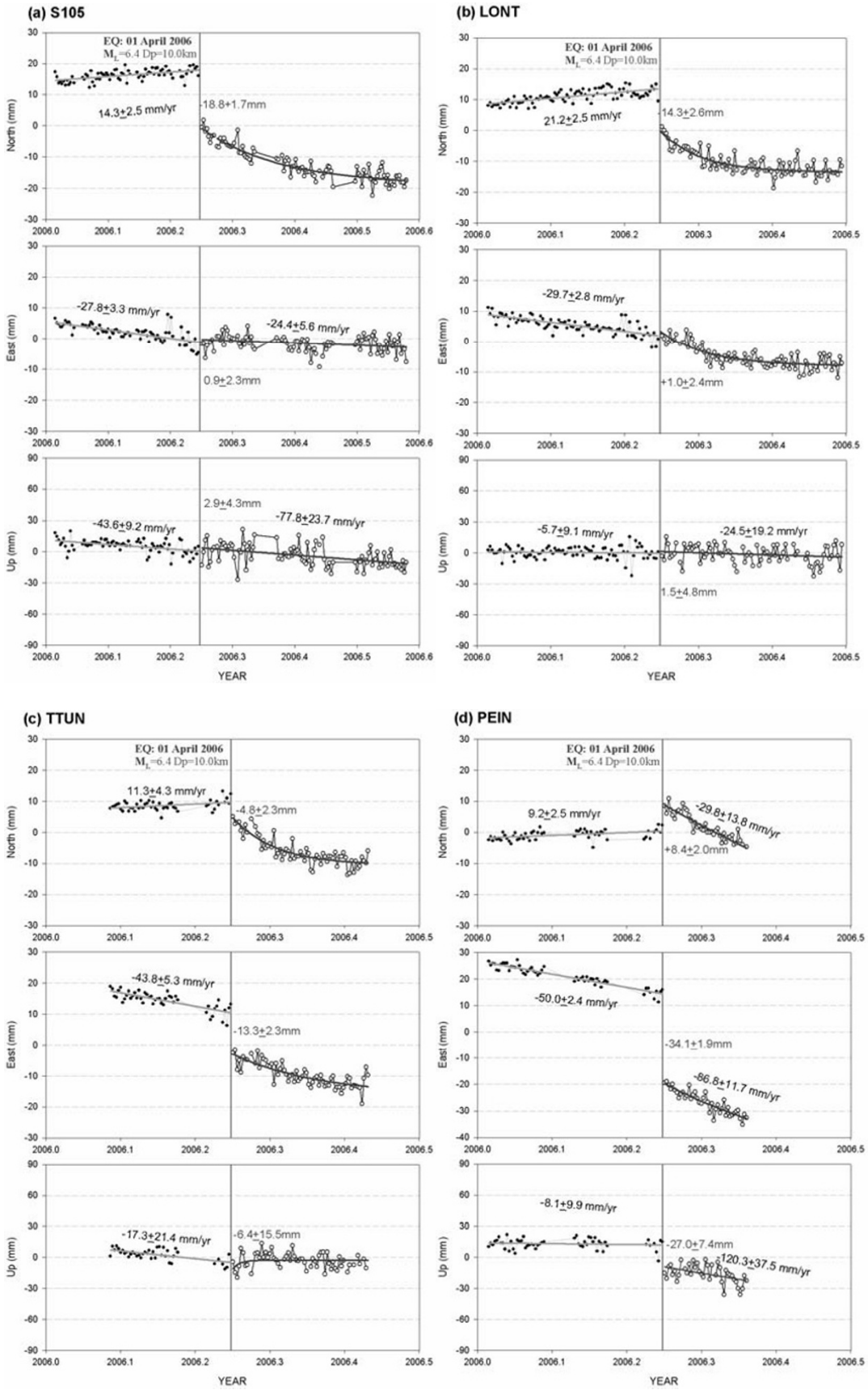

Fig. 3. The time series of daily solutions from the six CGPS sites in the study area. Four different slip behaviors, including co- and postseismic displacements, can be observed among the six CGPS stations. Stations S105 (a) and LONT (b) represent the displacement behavior close to the epicenter; stations TTUN (c) and PEIN (d) represent that along the southern portion of the Y fault; station ERPN (e) represents that at some distance from the epicenter to the north and northeast; station S104 (f) represents that at some distance away from the epicenter to the southeast and also affected by a major aftershock that triggered the slippage on the LVF. See details about the co- and postseismic slip behaviors in each different region in the text.

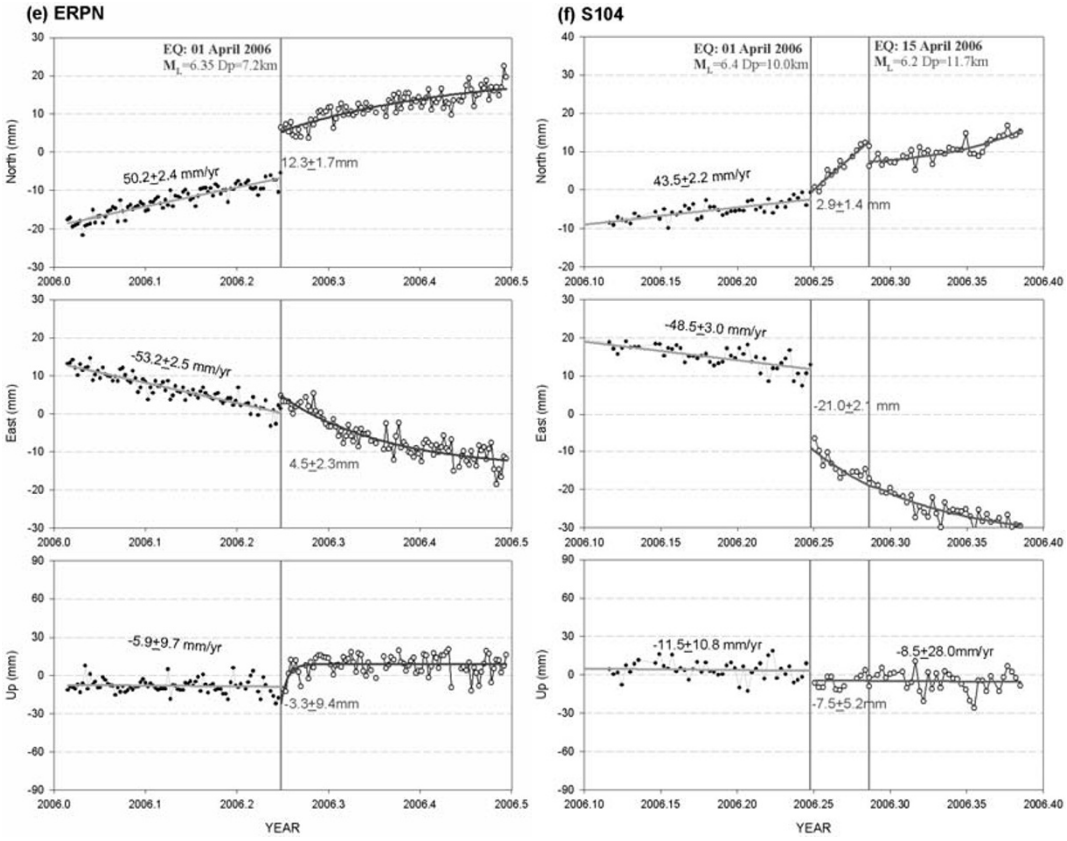

Fig. 3. (continued).

campaign-mode GPS sites (CMS) that had been surveyed repeatedly since 2001.

3.1 Continuously recording GPS stations

The standard data processing procedures for CGPS stations in CORS consist of two parts (Chen *et al.*, 2003): (1) single epoch solutions and (2) daily solutions. The data logging of CGPS use a dual sampling rate system of 30 s and 1 s. As an earthquake occurs, both the single-epoch solution estimated by 1-Hz (1 s) data (Fig. 2) and the daily solution from 30-s data (Fig. 3) are processed following the standard procedures of the Bernese V4.2 software (Hugentobler *et al.*, 2001).

Measurements from seven CGPS stations near the epicentral area of the Peinan earthquake (Fig. 1) were used for determining and characterizing the surface displacements associated with the Peinan earthquake. We applied a linear regression algorithm to estimate the interseismic velocity and an exponential decay algorithm to fit the postseismic displacements from daily solutions (Bock *et al.*, 2000; Yu *et al.*, 2003). The surface motions recorded by CGPS stations showed three main different behaviors of co- and postseismic movements around the epicentral area. First, two stations close to the epicenter (stations S105 and LONT; Fig. 3(a) and (b)) revealed a S-SSW coseismic displacement with a month-long exponential decay of a southward postseismic displacement. Second, two stations to the south of the epicenter and in the footwall of the Y fault in the Longitudinal Valley (stations TTUN and PEIN; Fig. 3(c) and 3(d)) indicated a westward (WNW-WSW) and downward coseismic displacement and a southward and upward postseismic displacement. Third, the station located away from the epicenter to the NE (station EPRN; Fig. 3(e)) showed a northward coseismic displacement with a westward and upward postseismic displacement. We also found that station S104 located farther to the SE in the southernmost Coastal Range exhibited a similar behavior of coseismic movement to stations TTUN and PEIN but an opposite NW postseismic displacement that was clearly also affected by a major aftershock sequence ($M_L = 5.7$) 14 days following the main shock in the offshore area (Fig. 3(f)). As mentioned above, this aftershock sequence appears to result from the rupture of the LVF. As a result, we interpret the data as indicating that the Peinan earthquake of the Y fault triggered the slippage along the LVF, especially the Lichi fault (the eastern branch of the LVF), so that the hanging-wall of the Lichi fault (e.g., station S104) would move differently from the footwall of the fault (i.e., stations PEIN and TTUN) during the post-seismic period (compare Fig. 3(c) and 3(d) with 3(f)). Based on the data for the above-surface motion as related to the earthquake together with the aforementioned major geological structures, we divide the study area into four terrains, each revealing its distinct surface deformation behavior: (a) epicenter area; (b) south of the epicenter area; (c) NE away from the epicenter area; (d) SE away from the epicenter area on the hanging-wall side of the Lichi fault. We will come back to discuss this in more detail in the next section using the results of the campaign GPS measurements.

The list of coseismic displacements recorded by the selected seven CGPS sites around the epicenter area associ-

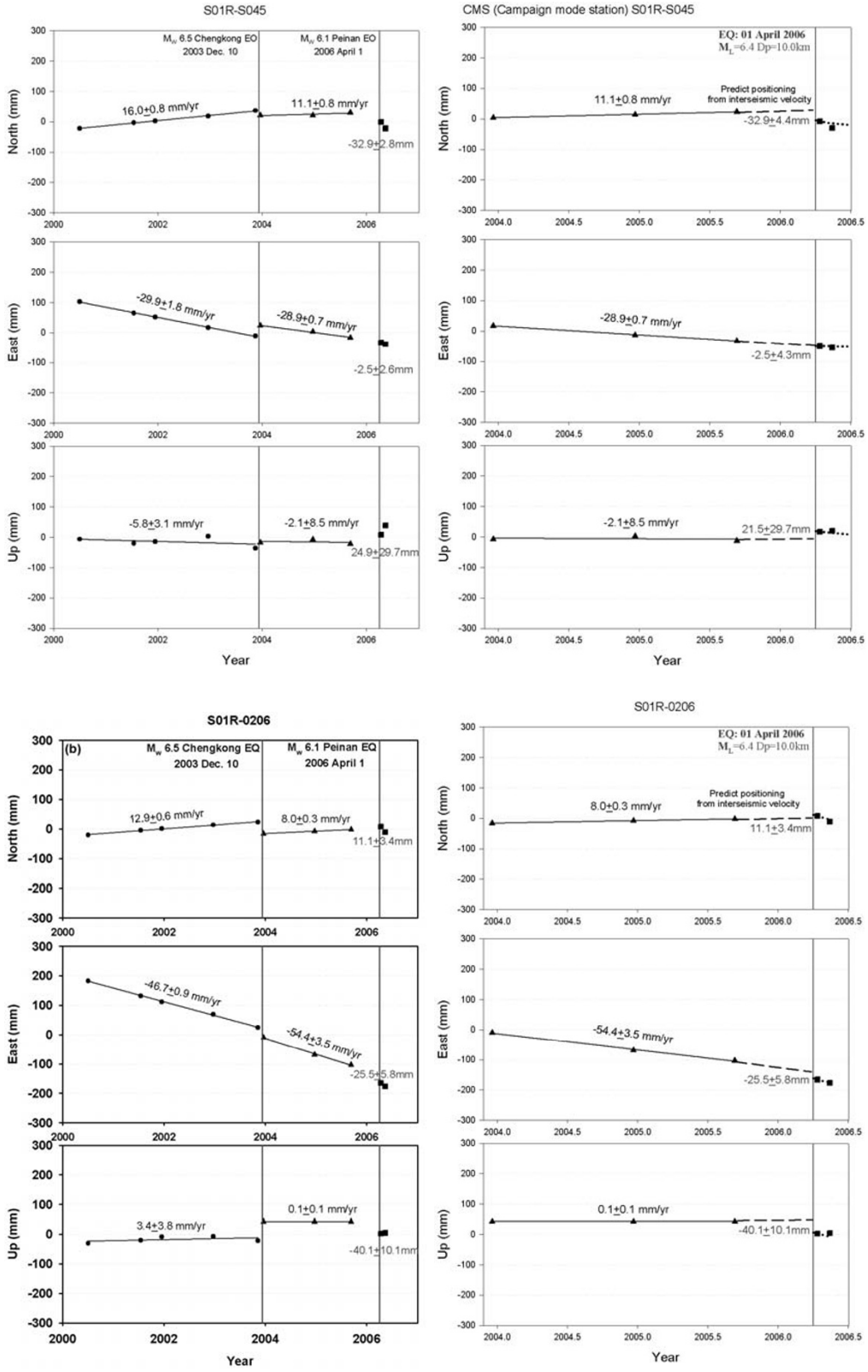

Fig. 4. Examples of the estimation of pre-seismic secular velocity for campaign-mode GPS time series in the study area. The displacements are relative to station S01R. The vertical line in each subplot shows the epoch of the Peinan earthquake. Interseismic velocity is determined by a linear fitting of annual measurements before the earthquake between 2001 and 2005.

ated with the 2006 Peinan earthquake are shown in Table 1.

3.2 Campaign-mode sites

As mentioned above, along the southern LVF, a GPS network consisting of 52 CMS has been surveyed annually since December 2001 (Table 2). Most of the CMS were occupied at least six times before and one or two times after the main shock of the 2006 Peinan earthquake. In each campaign session, 8–12 stations were occupied simultane-

Table 1. Results of the surface coseismic displacements and standard deviations derived from the seven continuous GPS stations around the epicentral area of the 2006 Peinan earthquake.

Station	Latitude (°)	Longitude (°)	dN (mm)	dE (mm)	dU (mm)
ERPN	22.9440	121.1580	12.3 ± 1.7	4.5 ± 2.3	−3.3 ± 9.4
LONT	22.9081	121.1225	−14.3 ± 2.6	1.0 ± 2.4	−1.5 ± 4.8
PEIN	22.8029	121.1151	8.4 ± 2.0	−34.1 ± 1.9	−27.0 ± 7.4
S104	22.8226	121.1813	2.9 ± 1.4	−21.0 ± 2.1	−7.5 ± 5.2
S105	22.9535	121.1048	−18.8 ± 1.7	0.9 ± 2.3	2.9 ± 4.3
SINL	22.9101	121.2466	0.6 ± 1.6	1.6 ± 2.5	−13.6 ± 10.2
TTUN	22.7664	121.0726	−4.8 ± 2.3	−13.3 ± 2.3	−6.4 ± 15.5

Table 2. Summary of GPS campaigns in the southern Longitudinal Valley area between 2001 and 2006. Note that the Peinan earthquake occurred on Day 91, 2006, shortly before Campaign 7.

Campaign	Survey period (DoY)	Stations	Session (h)	Instrument
1	345–350, 2001	44	7	Trimble 4000 SSE/SSI
2	351–357, 2002	49	7	Trimble 4000 SSE/SSI
3	308–314, 2003	52	8	Trimble 4000 SSE/SSI
4	082–091, 2004	52	13	Trimble 4000 SSE/SSI
5	349–360, 2004	52	13	Trimble 4000 SSE/SSI
6	249–258, 2005	52	13	Trimble 4000 SSE/SSI
7	102–105, 2006	18	13	Trimble 4000 SSE/SSI
8	129–141, 2006	52	13	Trimble 4000 SSE/SSI

ously with dual-frequency GPS receivers and observation were made for 7–13 h. The sampling rate was 15 s, and the elevation cutoff angle was 10°. The raw data are transferred to the RINEX (Receiver INdependent EXchange) format for post-processing. Before each campaign, adjustments of leveling and centering biases of the tribranches were conducted to minimize the instrumental errors. We also avoided or eliminated the environmental obstructions, such as trees or grass, to reduce the influences of multipath effects. During the post-processing of data, the daily solutions of nearby CGPS were incorporated into the determination of session solutions (Hugentobler *et al.*, 2001). The Penghu station, S01R, located at the stable Chinese continental margin in the Taiwan Strait, was adopted as the reference station to define the "minimum constrained conditions" to its value in the International Terrestrial Reference Frame 2000 (ITRF00).

Observing the results of Campaigns 1–6, which were carried out annually between 2001 and 2005 (i.e., before the 2006 Peinan earthquake), we found that the nearby 2003 $M_w = 6.5$ Chengkung earthquake only slightly affected the secular velocity in the study area, as illustrated by the very minor decrease in secular velocity for stations S045 and 0206 following the 2003 earthquake (Fig. 4). As a result, we intended adopting the three campaign measurements from March 2004 to September 2005 (Campaigns 4–6) to represent the secular preseismic motions for each CMS station in the study area. Campaigns 7 and 8, which were conducted within 2 months following the Peinan earthquake, were used to estimate coseismic surface displacements of the Peinan earthquake (Fig. 4). Due to the presence of some unnegligible postseismic deformation around the epicenter area—based on the aforementioned CGPS data—we were aware that the direct difference of station coordinates from session solutions before and after the earthquake can not be totally attributed to the coseismic displacement. It is thus necessary to correct secular motions due to the rapid interseismic movements and, more importantly, to remove the postseismic deformation in order to obtain the coseismic displacement. In this study, we applied two major procedures to obtain the CMS coseismic displacements. In the first step, the preseismic secular motions of 2004–2005 are corrected using the linear regression of velocities obtained in Campaigns 4–6 (Fig. 4). Secondly, we applied the postseismic displacement correction using the nearby CGPS data into Campaigns 7 and 8. Because of different postseismic behaviors being observed at CGPS stations, each CMS was categorized into the four geological regions discussed above. Figure 5 shows estimates of the co- and post-seismic displacements of CMS in four different regions by including the preseismic linear secular motion and the postseismic exponential decay. After correcting postseismic displacements for all 52 CMS using CGPS data (Fig. 5, Table 3), we found that misfits are relatively small for most of the CMS. As a result, we consider that our correction for postseismic displacements is, to some extent, reliable.

The results of the coseismic displacements for the CMS are listed in Table 4. The average precisions of the horizontal and the vertical components are about 5.4 mm and 16.6 mm, respectively.

4. Vertical Coseismic Displacements from Leveling Surveys

Six leveling routes have been deployed in the southern Longitudinal Valley area (Fig. 1), including five routes in the E-W direction (sub-perpendicular to the major structure features) and one route in the N-S direction (sub-parallel to the major structures). We used the elevation difference between the two leveling surveys, which were conducted 4–6 months before and 1–2 months after the main shock,

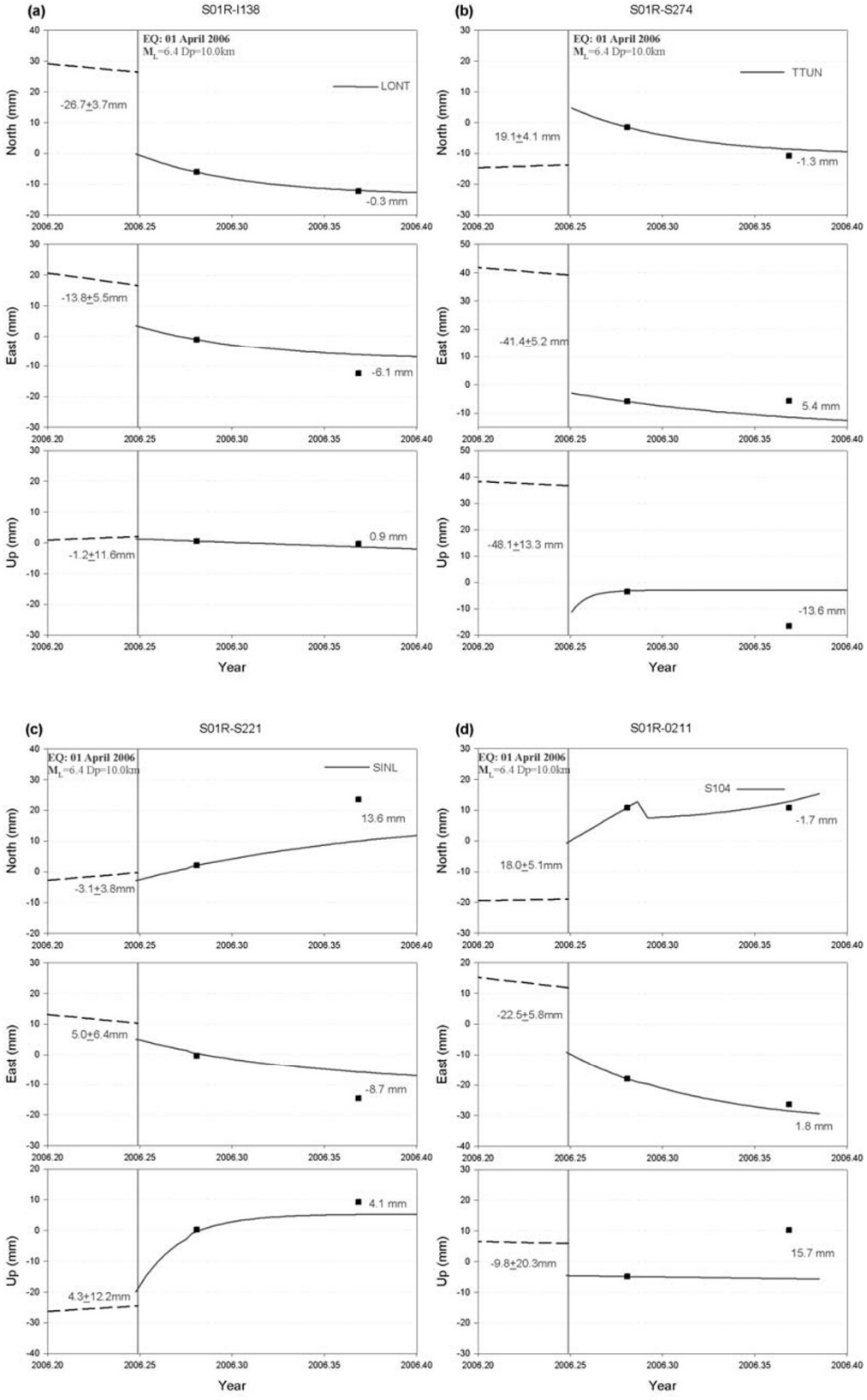

Fig. 5. Examples of estimates of co- and postseismic displacements from the campaign-mode GPS sites in four different regions. Coseismic displacements at CMS stations are corrected for postseismic displacements using the representative CGPS station in each region. Site I138 (a) used station LONT near the epicenter area. Site S274 (b) used the station TTUN in the southern part of the Y fault. Site S221 (c) used station SINL located northeast away from the epicenter. Site 0211 (d) used the station S104 located southeast away from the epicenter.

Table 3. Misfits of the postseismic deformation on the campaign CMS by adopting postseismic decay behavior from nearby CGPS in three different regions: (a) epicentral area, (b) southern part of the Y fault, (c) hanging-wall of the Lichi fault, (d) north, away from the epicenter. △N, △E, △U: misfits of each CMS in the north, east, and up components, respectively. Black star in CGPS column: alternative CGPS with slightly bigger misfits.

(a) Epicentral area (CGPS: LONT and S105)

CMS	△N (mm)	△E (mm)	△U (mm)	CGPS
I138	−0.3	−6.1	0.9	LONT
S045	−14.5	−5.0	−3.9	S105
S126	6.0	−3.4	−18.1	LONT
S211	−8.6	−2.0	5.2	S105
S212	2.8	−11.8	5.7	LONT
S215	−6.6	−3.3	4.9	LONT
S216	−15.7	−3.3	−15.1	LONT
S217	−0.3	−6.1	14.8	LONT
S219	−12.5	5.2	−11.0	LONT
S237	−0.2	−0.5	−4.2	LONT
W048	−0.2	−3.3	−7.1	LONT
MEAN	−4.6±7.4	−3.6±4.1	−2.5±10.0	
I138	0.6	−10.5	3.3	S105★
S045	−15.6	−0.6	−6.3	LONT★
S126	6.9	−7.8	−15.7	S105★
S211	−9.5	2.4	2.8	LONT★
S212	3.7	−16.2	8.1	S105★
S215	−5.7	−7.7	7.3	S105★
S216	−14.8	−7.7	−12.7	S105★
S217	0.6	−10.5	17.2	S105★
S219	−11.6	0.8	−8.6	S105★
S237	0.7	−4.9	−1.8	S105★
W048	0.7	−7.7	−4.7	S105★
MEAN	−4.0±7.8	−6.4±5.5	−1.0±9.8	

(b) Southern part of the Y fault (PEIN and TTUN)

Name	△N (mm)	△E (mm)	△U (mm)	CGPS
0206	−8.9	−2.4	11.6	PEIN
S274	−1.3	5.4	−13.6	TTUN
MEAN				
0206	−11.5	−1.0	2.7	S104★
S274	0.3	9.0	−3.4	PEIN★
MEAN				

(c) Hanging-wall of the Lichi fault (S104)

Name	△N (mm)	△E (mm)	△U (mm)	CGPS
0207	−1.7	−9.5	−16.4	S104
0211	−1.7	1.8	15.7	S104
S054	−1.6	4.7	−5.3	S104
S218	−1.7	7.5	−6.3	S104
MEAN				
0207	9.7	−10.9	−7.5	PEIN★
0211	−7.1	−2.9	14.7	TTUN★
S054	9.8	3.3	3.6	PEIN★
S218	5.9	2.4	−5.1	LONT★
MEAN				

(d) North away from the epicenter (ERPN and SINL)

Name	△N (mm)	△E (mm)	△U (mm)	CGPS
S221	13.6	−8.7	4.1	SINL
S221	16.9	−6.5	8.7	ERPN★

Table 4. Results of the surface coseismic displacements of the 2006 Peinan earthquake and standard deviations derived from the 52 campaign-mode sites (CMS).

Stations	Latitude (°)	Longitude (°)	*d*N (mm)	*d*E (mm)	*d*U (mm)
0206	22.8117	121.1012	11.1± 3.4	−25.5±5.9	−40.1±10.1
0207	22.8196	121.1395	14.1± 5.5	−42.6±6.1	−23.3±14.5
0211	22.7553	121.1340	18.0± 5.1	−22.5±5.8	−9.8±20.3
0308	22.9440	121.1528	13.3± 6.4	−0.3±3.3	5.7±14.1
8049	22.9476	121.1290	−10.3± 6.7	−2.6±4.1	28.3±10.8
8050	22.9268	121.1361	−1.9± 4.1	6.5±7.9	17.8±10.3
9172	22.9336	121.1371	11.4± 8.8	1.3±3.9	3.4±26.6
I138	22.8665	121.1012	−26.7± 3.7	−13.8±5.5	1.2±11.6
S044	22.6796	121.0144	−7.9± 4.0	−14.6±4.1	−2.2±14.4
S045	22.8821	121.0724	−32.9± 4.4	−2.5±4.3	21.5±29.7
S054	22.7958	121.1894	16.8± 3.2	−28.4±5.1	−15.1±19.9
S057	22.9748	121.3011	7.7± 5.1	−1.6±6.1	−50.1±14.5
S072	22.9274	121.1545	4.8± 7.2	−9.6±7.2	−7.7±14.0
S126	22.8919	121.1423	−18.4± 4.7	4.5±3.3	−13.2±19.8
S127	22.9434	121.1444	8.6± 3.7	−4.5±3.2	−13.5±18.8
S128	22.9420	121.1491	2.1± 7.6	1.8±6.9	−17.3±12.2
S193	22.9428	121.1608	4.5± 7.6	8.6±4.7	−6.5±13.2
S194	22.9447	121.1561	−1.8± 4.7	8.3±3.9	5.8±19.8
S195	22.9337	121.1278	8.3± 7.6	−1.2±7.1	13.7±18.1
S196	22.9366	121.1245	5.9± 4.4	−1.3±6.5	21.8±15.7
S197	22.9392	121.1201	−5.0± 6.9	3.5±5.0	21.1±18.5
S198	22.9405	121.1187	−4.3± 3.5	−2.1±5.0	15.3±15.9
S199	22.9075	121.1277	−7.4± 4.2	0.6±3.5	−18.3±18.3
S200	22.9055	121.1171	−18.0± 4.8	0.4±4.1	−3.9±16.9
S201	22.9058	121.1087	−18.0± 4.5	−1.9±4.5	−15.9±13.0
S203	22.9060	121.1031	−25.0± 4.2	−2.4±6.9	−17.3±12.1
S205	22.9097	121.0846	−41.5± 7.5	1.4±7.8	−17.1±13.4
S206	22.9158	121.0838	−34.4± 4.0	−8.7±3.1	−21.7±12.2
S207	22.9416	121.1165	−13.4± 4.8	1.9±3.1	13.3±11.1
S209	22.9039	121.0730	−37.9± 4.4	−11.2±6.4	−11.0±28.9
S211	22.8824	121.0868	−34.1± 8.1	2.3±7.0	2.6±19.4
S212	22.8709	121.1328	−22.8± 8.9	−6.4±6.8	−25.0±12.8
S213	22.9191	121.1147	−7.8± 9.5	−2.7±3.7	−1.4±38.2
S214	22.9648	121.2324	9.9± 4.5	3.6±6.4	−10.3±28.8
S215	22.8758	121.1025	−33.6± 4.5	−6.7±4.1	19.3±33.7
S216	22.8733	121.1140	−22.1± 3.8	−5.7±4.0	10.9±15.8
S217	22.8698	121.1353	−5.1± 3.1	−10.3±7.2	−13.5±18.8
S218	22.8676	121.1488	−9.1± 3.2	−2.7±9.8	−17.3±12.2
S219	22.8792	121.1097	−17.8± 5.6	−2.2±5.7	10.9±15.8
S221	22.9301	121.2608	−3.1± 3.8	5.0±6.4	4.3±12.2
S232	22.9448	121.2090	10.5± 3.2	−2.0±5.4	31.0±11.3
S237	22.8995	121.1414	−11.8± 3.5	−1.8±6.7	−1.3±16.1
S238	22.9059	121.1063	−18.8± 4.5	1.0±4.5	−6.8±13.0
S239	22.9071	121.0933	−19.1± 4.0	−6.5±6.2	−13.0±12.2
S240	22.9009	121.0539	−37.5± 5.8	4.9±7.8	12.2±34.5
S241	22.8943	121.0402	−34.0± 7.3	−4.9±9.3	26.2±18.6
S245	22.9808	121.1292	−1.8± 4.5	−0.5±6.0	2.3±13.2
S248	22.9773	121.1786	6.2± 4.4	−12.0±4.6	−3.2±14.1
S274	22.7804	121.1005	19.1± 4.1	−41.4±5.2	−48.1±13.3
V108	22.9757	121.1491	−1.4± 4.7	4.6±5.5	−26.3±18.8
V109	22.9747	121.1663	−1.2± 5.5	−5.0±5.6	15.4±17.6
W048	22.9031	121.1457	−11.7±10.5	7.3±5.2	5.9±10.7

to examine the vertical motion associated with the 2006 Peinan earthquake (Table 5).

In this study, we incorporated the leveling measurements with results of the coseismic vertical components obtained from CGPS data, including stations S104, TTUN, LONT, S105, and ERPN, along the leveling routes, with the exception of Route 5 away from the epicentral area. The comparison shows a good agreement of coseismic movement between leveling and GPS vertical measurements for a difference of less than 10 mm, except for station ERPN, where

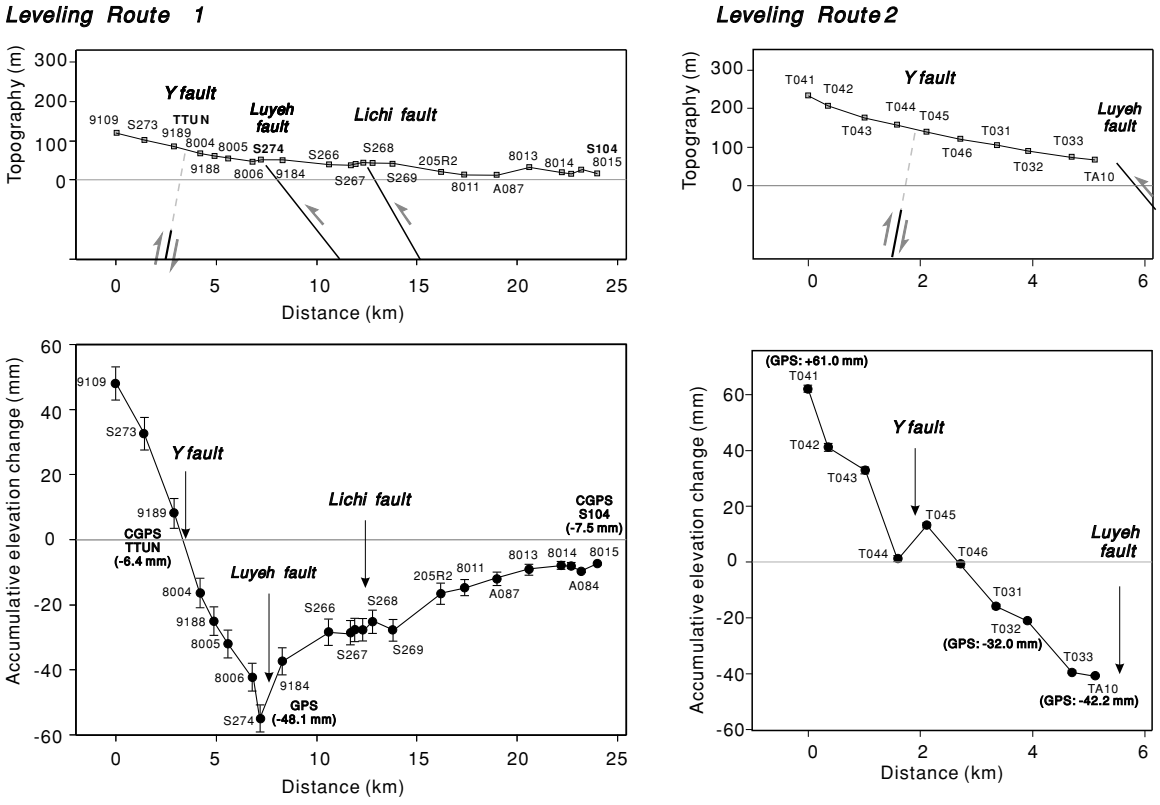

Fig. 6. Precise leveling results of Routes 1 and 2 in the southern part of the rupture area. The upper and lower panels show the elevation and the cumulative elevation changes, respectively. The coseismic movements of the CGPS with respect to the stable Chinese continental margin have been used as the reference for determining the coseismic vertical motion. There was a substantial vertical movement of at least 100 mm at a distance of 7 km across the Y fault. Elevation changes across the two branches of the LVF (i.e., the Luyeh fault and the Lichi fault) indicated that small amounts of slip that occurred might be triggered by an aftershock sequence. See the text for details.

significant postseismic vertical motion occurred. As a consequence, we adopted the vertical coseismic displacements at the continuous GPS station S104 as a reference, thereby obtaining the coseismic vertical movements for each benchmark along the leveling routes.

4.1 Taitung-Peinan area: the southern part

We found that vertical movements on the benchmarks close to the epicenter were absent, which is in contrast to the large signals found along the southern part of the Y fault. South of the epicentral area, leveling Route 1, which is 25 km long and extends across the southernmost part of the Longitudinal Valley, has previously been observed several times from 1984 to 1988 (Yu *et al.*, 1992). The results of these authors showed that there was only a small amount of relative vertical motion, 5–6 mm/year, across the southern end of the Longitudinal Valley, from the foot of the Central Range to the west side of the Coastal Range. Consistent with these results, recent vertical displacements of CGPS stations in this area between 1993 and 2006 (i.e., TTUN and S104) also showed no obvious vertical movement before the 2006 earthquake.

The coseismic elevation change of leveling Route 1 shows a significant vertical movement associated with the Peinan earthquake, especially from the eastern margin of the Central Range to the western half of the valley (Fig. 6(a)). In more detail, we can observe several features, from west to east: (1) there is at least a 50-mm westward uplift in the eastern margin of the Central Range (from station 9189 to 9190); (2) there is more than 50-mm movement, in a sharp east downward direction, from the foot of the Central Range (station 9190) to the middle of the valley (S274); (3) a 50-mm gradual uplift occurred from the middle of the Valley (S274) to the eastern side of the Coastal Range (8015). In summary, the coseismic vertical movement shows an asymmetric pattern: a steeply downward movement of more than 100 mm in the western part of the valley and a smoothly upward movement of 50 mm in the eastern part. Note that the above-mentioned elevation change occurred between 4 months prior to and 2 months after the earthquake; thus, the postseismic displacements and/or triggered motion on other faults, such as the Lichi fault, would be included in the result.

Leveling Route 2, a few kilometers north of Route 1 with a much shorter distance of 5 km, extends eastward from the foot of the Central Range to the middle of the valley. We compared the measurements 5 months prior to and 1 month after the earthquake to obtain the coseismic movements. An analysis of leveling Route 2 (Fig. 6(b)) shows a similar pattern of motions as those found for leveling Route 1—that is, an upward movement of about 60 mm in the hanging wall of the Y fault and a downward movement of about 40 mm in the footwall. The total cumulative elevation change of 100 mm occurred across the Y fault on the western side of the valley.

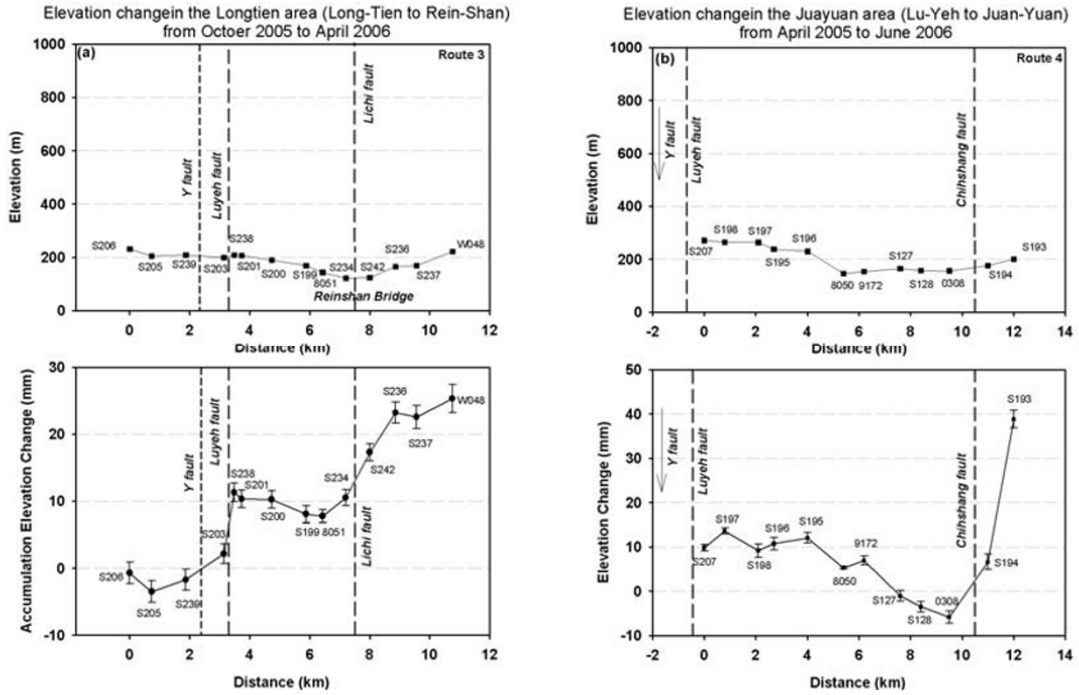

Fig. 7. Precise leveling results of Route 3 (a) and Route 4 (b) near the epicentral area (Luyeh area). The upper and lower panels indicate the elevation and the cumulative elevation changes, respectively.

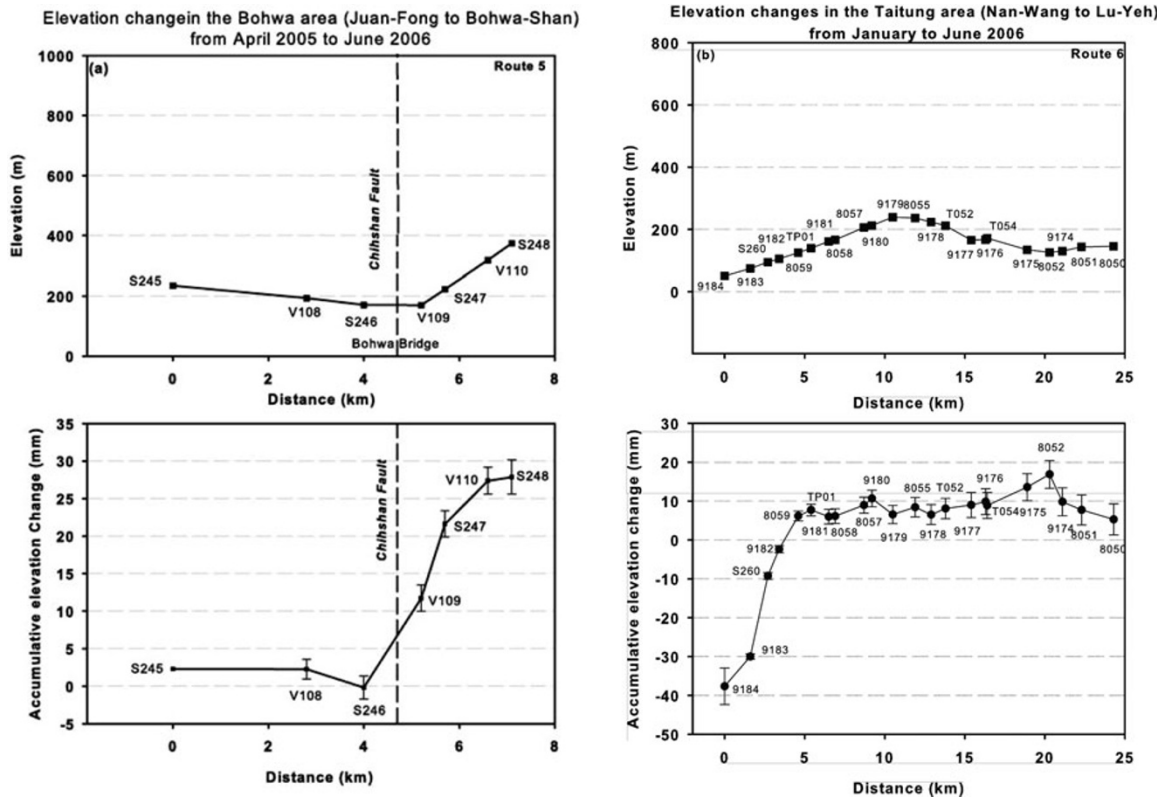

Fig. 8. Precise leveling results of Route 5 (a) north from the epicenter (Baowa area) and (b) the N-S-trending Route 6, which closely follows the surface projection of the Y fault between the Central Range and the Peinanshan massif. The elevation changed drastically in Route 6 near the southern end of the route, where it turns southeast away from the Y fault.

4.2 Luyeh area: the epicentral area

Near the epicenter, two sub-parallel leveling routes (Routes 3 and 4, each 11–12 km long) in the Luyeh area run mainly across the Longitudinal Valley (Fig. 1). The CGPS observed that the coseismic elevation change between ERPN and S105 is almost negligible, which is about 25–30 mm less than the leveling results along Route 4. In fact, the continuous GPS recording of ERPN indeed re-

vealed a significant postseismic vertical motion (Fig. 3(e)), implying that non-negligible postseismic deformation occurred along leveling Route 4 and, most likely, Route 3 as well. We tend to interpret this postseismic deformation as being mainly due to triggered slippage on the LVF, including the two branches of the Luyeh fault and the Lichi fault.

In Fig. 7, the vertical displacements of the leveling routes in the Luyeh area can be seen to exhibit obvious surface motion, which may be associated not only with the coseismic faulting of the Peinan earthquake but also with triggered slips on the nearby LVF. For example, leveling Routes 3 and 4 across two major branches of the LVF, the Luyeh fault and the Lichi fault, both show about 10 mm of uplift across each fault. Note that the M_L 5.6 aftershock sequence did occur on the LVF 2 weeks following the main shock. Nevertheless, interseismic creep of the Luyeh fault and the Lichi fault, which was estimated to be about 10 mm/year and 20 mm/year (Chen *et al.*, 2004), respectively, may also have contributed to the vertical uplift of the leveling measured in a time span of 5–7 months. As for the Y fault, which was the causative fault of the Peinan earthquake, leveling Route 3 did not indicate a significant vertical motion (Fig. 7(a)) across the eastern margin of the Central Range (i.e., presumably the surface projection of the Y fault), indicating a limited minor coseismic down-dip slip in addition to a dominant left-lateral motion on the Y fault.

4.3 Baowa area: north of the epicentral area

Leveling Route 5, which is located farther north of the epicentral area, runs in the E-W direction across the southern end of the Chihshang fault (belonging to the LVF) near the foot of the hills of the Coastal Range. We compared two measurements in a time span of 14 months, 12 months before and 2 months after the main shock, to discuss the vertical movements associated with the 2006 Peinan earthquake. As there is no CGPS station along this leveling route, we used the nearby CMS station as the reference to reconstruct the elevation changes of Route 5 (Fig. 8(a)).

We were able to observe a significant uplift of about 25 mm across the Chihshang fault near the Baowa bridge that is generally consistent with the interseismic secular movement of the fault (Yu and Liu, 1989; Angelier *et al.*, 1997; Lee *et al.*, 2003). We tend to interpret the event as indicating that vertical motion was not significantly affected, if at all, by the 2006 Peinan earthquake in the Baowa area.

4.4 N-S cross section

The 25-km-long N-S trending leveling Route 6 follows the western margin of the Peinanshan massif, Plio-Pleistocene fluvial deposits in the middle of the valley. In terms of the Peinan earthquake, leveling Route 6 seemingly runs parallel along or near the surface projection of both the Y fault and the Luyeh fault. The result of coseismic elevation change (Fig. 8(b)) shows that there is an abrupt downward motion in the southern end of the leveling route, where the route turns SE away from the Y fault. A downward movement of about 40 mm was observed in a short distance of 5 km, which is consistent with the data obtained on the nearby Route 2. In contrast, only a slight vertical motion within 10 mm was observed across the northern part of the Peinanshan massif, which we interpret to be triggered slippage on the Luyeh fault.

5. Results of Coseismic Displacements from GPS and Leveling Measurements

By combining the results from continuous and campaign GPS stations as well as leveling measurements, we were able to construct a map of the coseismic horizontal and vertical displacements in the epicentral area near the southern Longitudinal Valley (Fig. 9; Tables 1, 3 and 4).

As revealed by Fig. 9(a), the surface coseismic horizontal displacements can be divided into three distinct patterns in three areas. Note that the map has been divided into four areas taking both co- and postseismic displacements patterns into account, as mentioned in Section 3.2. Namely, the area extending south of the epicenter and that far to the SE showed similar coseismic displacements although they illustrated distinct postseismic behaviors. Firstly, close to the epicentral area (middle part of the map shown in Fig. 9(a)), the horizontal displacements show a S-SSW movement of 10–45 mm. The vectors are located in the Central Range (i.e., on the hanging wall of the Y fault) and show a larger amount of displacement relative to those in the valley (the footwall of the fault), indicating a left-lateral strike slip along the Y fault, which is consistent with the focal mechanism of the main shock. Secondly, the region south of the epicenter shows a westward motion of 30–40 mm in the footwall of the Y fault and a SSW movement of 40–45 mm in the hanging wall. This implies a significant horizontal shortening in addition to the left-lateral slip across the causative Y fault of the earthquake in its southern portion. Taking the coseismic horizontal displacements in the above two regions into account, it would appear that the Y fault exhibits two distinct coseismic slip-rupturing between the northern and southern portions. This also raises the possibility that an E-W- or WNW-ESE-trending right-lateral faulting, located across the middle-north of the Peinanshan massif (Fig. 9(a)) occurred during the main shock. The surface projection of this potential E-W fault would separate the SSW vectors to the north and the WNW vectors to the south. Finally, in the region to the NE of the epicenter, the displacements are less than 15 mm in the direction between NW and NE. We interpret these small amounts of displacements as indicating a region that is located far from the effect of the causative Y faulting and/or the possible E-W-trending fault.

The coseismic vertical displacements (Fig. 9(b)), which represent the combined GPS and leveling measurements, show that there were no significant coseismic vertical movements except for those around the southern part of the Y fault, where the maximum uplift and subsidence are about 60 mm and −60 mm, respectively. The vertical movements in the northern and southern parts of the Y fault indeed shows a different slip behavior of faulting, indicating a dominant strike-slip motion in the north and a substantial thrust slip in the south.

In summary, taking into consideration the data on the coseismic horizontal and vertical displacements and the seismological information, including the focal mechanism of the main shock and the distribution of the aftershocks, we suggest that the 2006 M_w 6.1 Peinan earthquake likely ruptured the NNE-trending Y fault along a length of 20–25 km underneath the eastern margin of the Central Range. This

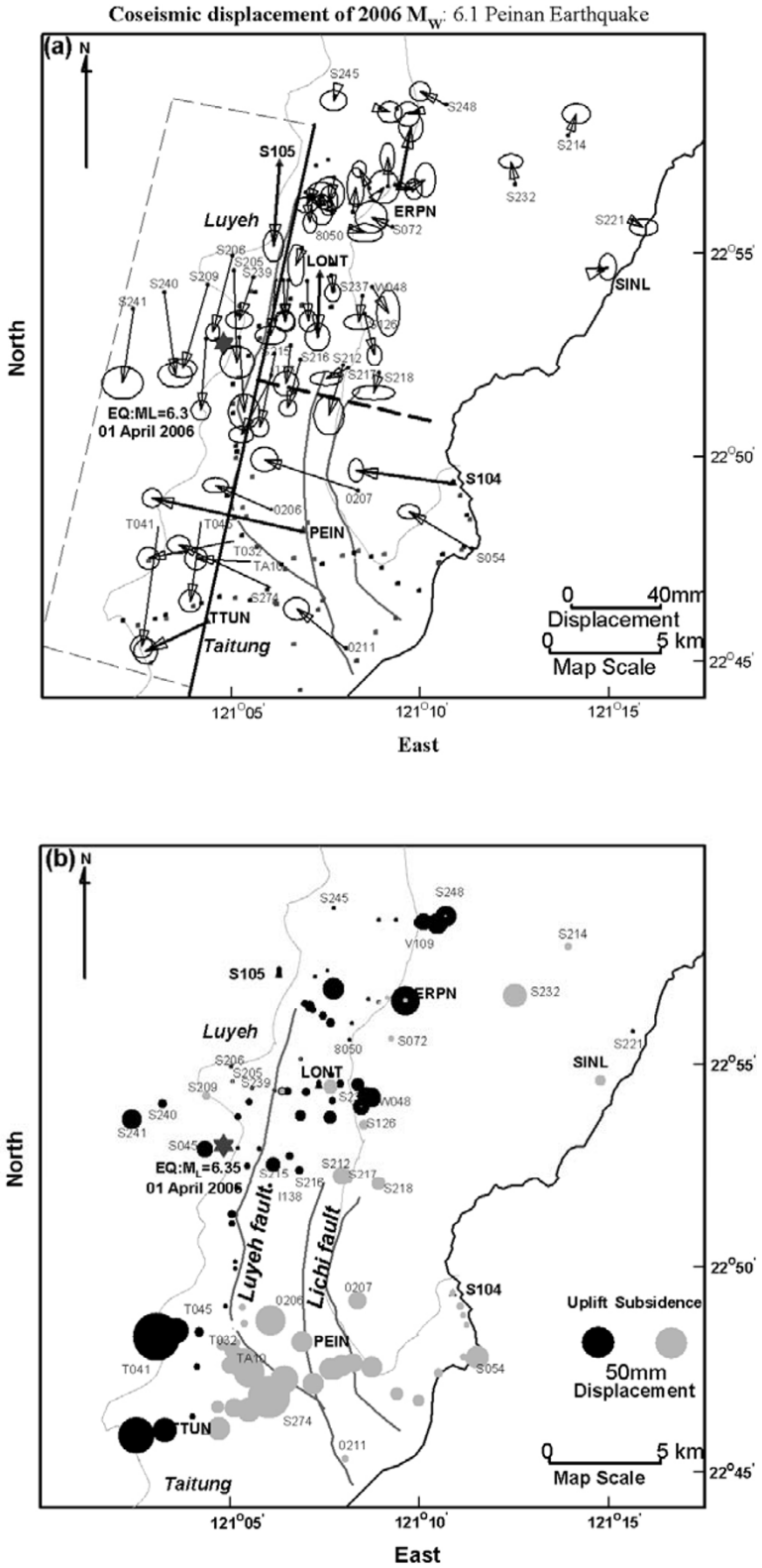

Fig. 9. Results of the horizontal (a) and vertical (b) coseismic displacements of the 2006 Peinan earthquake derived from combining all CGPS and CMS sites and leveling measurements. The heavy GPS vectors indicate the CGPS results. Star denotes the epicenter.

previously suspected fault corresponds to a cluster of aftershocks that formed a NNE-trending plane with a steep dip to the west (Wu *et al*., 2006). However, the GPS and leveling coseismic displacements indicate substantial heterogeneity of slip along the Y fault: a small amount of left-lateral motion in the north near the epicenter in contrast to a large amount of oblique reverse faulting with a significant left-lateral slip (Fig. 9). It is worthy noting that there was an apparent discrepancy in surface deformation between the north and south, suggesting that possibility that

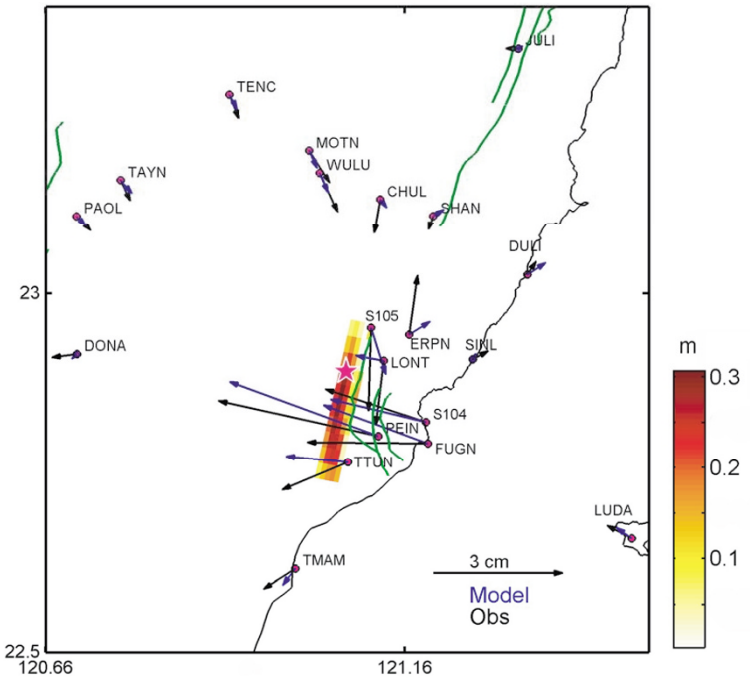

Fig. 10. Coseismic slip distribution projected on the surface is shown in color. Black and blue vectors indicate observed and predicted GPS displacements, respectively. Major faults are indicated as green solid lines. The magenta star is the epicenter of the main shock.

other coseismic ruptures of right-lateral slip occurred along the northern middle Peinanshan massif. In terms of the distribution of the aftershocks, there were indeed numerous aftershocks which occurred at the westernmost tip of this E-W discontinuity. However, no clear E-W-trending plane structure can be delineated from the aftershock distribution, suggesting that there may have been a series of E-W right-lateral faults over a broad zone. However, further investigations are needed to clarify this possible E-W-trending fault zone. A study of focal mechanisms of this cluster of aftershocks would be a great help; however, such a study is beyond the scope of this study.

6. Fault Geometry and Coseismic Slip Distribution

6.1 Model description

The focal mechanism of the main shock of the 2006 Peinan earthquake showed strike-slip faulting. Wu *et al.* (2006) proposed a high-angle, N-S-trending fault (CNF in their study) dip to the west (i.e., the Y fault in the present paper), and their model of fault geometry is generally consistent with surface displacements determined from sparsely distributed strong motion data. Based on much dense GPS data coverage and several leveling route measurements, we observed that the coseismic surface deformation is more complex. The coseismic horizontal displacement of about 10–20 mm to the north of the Peinanshan massif, around the epicenter area, are S-SSW directed; while coseismic displacements to the south increase in magnitude to about 20–40 mm, starting to move in the WNW direction on the footwall side of the Y fault (Fig. 9). The vertical displacements show a similar pattern, with a larger uplift and subsidence of about +60 mm to −60 mm, respectively, south of the epicenter than north (+15 mm to −10 mm). In addition, the relocated seismicity (Fig. 1) shows that a large number of aftershocks occurred around the northern Peinsnshan massif. The dramatic change in coseismic movements and the aftershock distribution suggest that the behaviors of the fault slip vary significantly from north to south.

We used all of the observed geodetic displacements, including CGPS and CMS data and the leveling measurements in an inversion to obtain the coseismic slip distribution associated with the 2006 Peinan earthquake. The modeled fault corresponds to the Y fault, which approximately follows the distribution of the aftershocks and the main shock. We assumed a fault dip of 80° to be consistent with the aftershock distribution and search for the rest of fault parameters, such as depth and width. We then inverted the fault parameters and coseismic slip distribution using a weighted least-square algorithm (Menke, 1984):

$$F(\mathbf{s}, \beta, \mathbf{m}) = \|\mathbf{W}(G(\mathbf{m})\mathbf{s} - \mathbf{d})\|^2 + \beta^{-2} \left\|\nabla^2 \mathbf{s}\right\|^2 \qquad (1)$$

where $\mathbf{s}$ is the coseismic slip, β serves as the weighting of the model roughness versus data misfit that is determined by cross-validation (Matthews and Segall, 1993), $\mathbf{m}$ is the fault geometry parameters, $\mathbf{W}$ is the weighting matrix and equivalent to the inverse square root of the data covariance matrix, $G(\mathbf{m})$ is Green's functions for the elastic half-space model (Okada, 1985), $\mathbf{d}$ is the observed GPS displacements, and ∇^2 is the Laplacian smoothing operator. To better account for the weights of GPS and leveling data, we first conducted two independent inversions using each data set separately. The weight in the joint inversion for each data set is then scaled by the reduced chi-square value from the initial independent models. The rescaling factor between

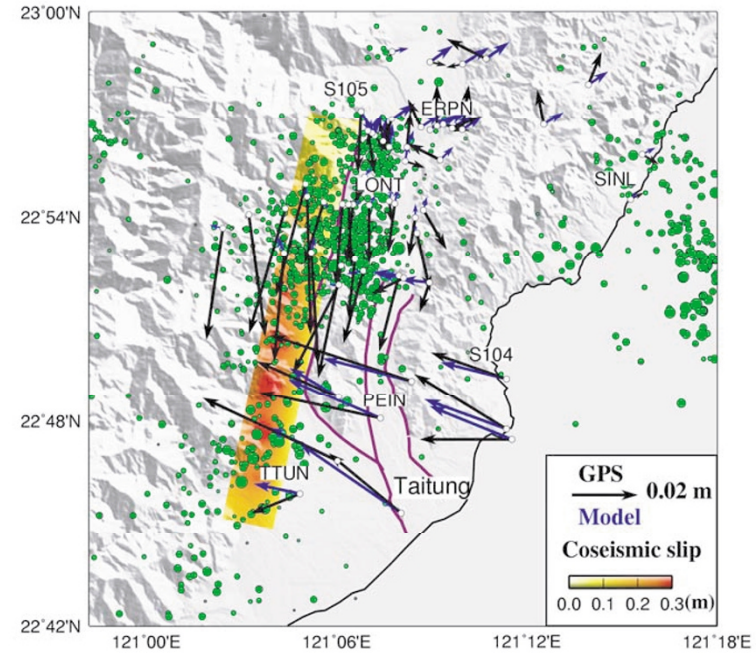

(a)

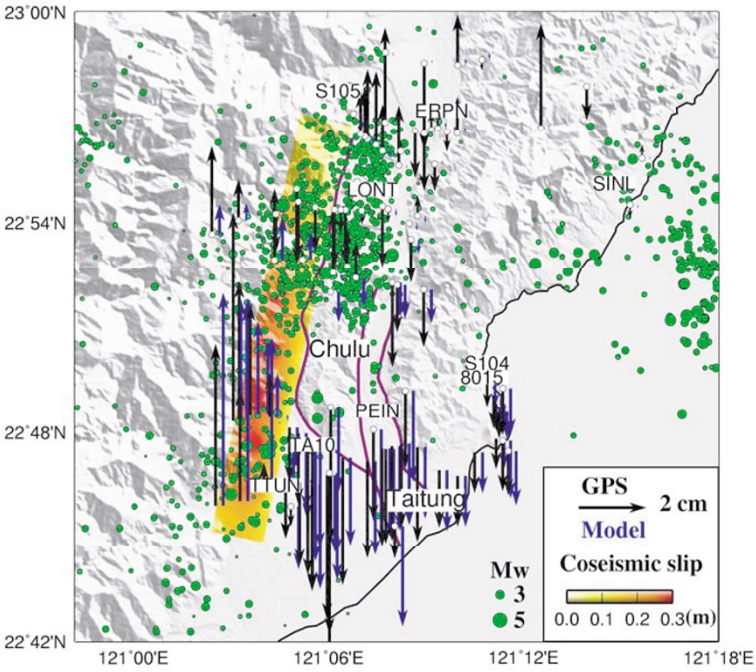

(b)

Fig. 11. (a) Coseismic slip distribution projected on the surface is shown in color. Black and blue vectors indicate observed and predicted GPS displacements, respectively. Major faults are indicated as solid lines. The white star is the epicenter of the main shock. Green dots denote relocated aftershocks from Wu *et al*. (2006). (b) Vertical displacements (black) and model predictions (blue).

the GPS data and the leveling measurements is 3 for the vertical movements.

As most CGPS sites locate on the footwall of the Y fault and show different characteristics of postseismic relaxation, the postseismic corrections of CMS displacements derived from CGPS sites may not be strictly justified, although their effects would be limited, as discussed in the previous section. Consequently, we decided to invert for two scenarios of coseismic slip distributions by (1) using only CGPS data and (2) using the whole data set (CGPS, CMS, and leveling). This event shows a strike-slip-dominated motion in the focal mechanism of the main shock. On the other hand, there was no evidence of clear surface rupture during the main shock, and no surface geological fault was recognized prior to the earthquake, suggesting that the coseismic rupture does not reach the surface and the fault is likely to be

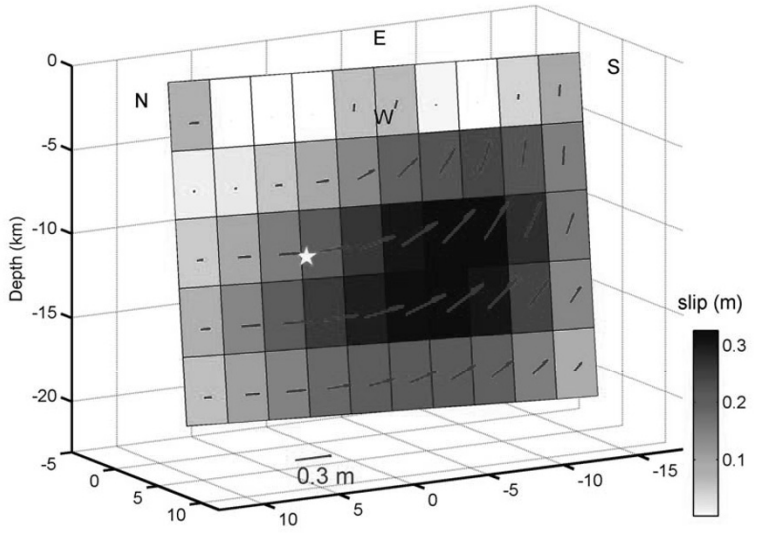

Fig. 12. The coseismic fault geometry and slip distribution. Slip on a 80° west-dipping fault between depths of 0.5 and 20 km. Color indicates coseismic slip. Blue vectors indicate fault slips. The white star is the hypocenter.

buried. Therefore, we searched the depth of the fault top from 0 to 5 km and the width from 10 to 25 km.

6.2 Modeling results from only CGPS data

We used all 19 available CGPS stations within a distance of 50 km from the epicenter (Fig. 10) for the first model. The optimal fault geometry, which was determined by grid search, shows a fault dip of 80° to the west at a depth range of 0.5–20 km. The surface projection of the modeled fault and fits of model predictions to CGPS displacements are shown in Fig. 10. The coseismic slip distribution showed a maximum slip of 0.3 m at depths of 12–16 km to the south of the hypocentral region (Fig. 10). The left-lateral motion dominates north of Peinsnshan massif, while up-dip motions are prominent to the south.

6.3 Modeling result from all GPS data and leveling measurements

For the second model, we used the identical fault geometry as determined by the inversion with only the CGPS sites described in the previous section. The fit of the model predictions to GPS and leveling measurements are shown in Fig. 11. The average misfits in horizontal and vertical displacements are 1.1 cm and 0.9 cm, respectively. The size of the misfit is rather reasonable given the surface displacements of 0.5 cm to a few centimeters around the epicenter area for a magnitude 6 earthquake. The data misfit on the northern section of the rupture is less satisfactory compared to that in the south. However, the residuals of horizontal and vertical displacements are mostly within the regions of 95% error ellipses. Along the optimal fault plane, the highest slip of about 0.33 m occurred at depths of 9–16 km on the southern portion of the fault (Fig. 12). The fault slip on the northern portion is mainly left-lateral, while it is primarily up-dip on the south portion (Fig. 12), which is consistent with the inversion using only CGPS data. The total geodetic moment in our modeled fault is 2.3×10^{18} Nt-m, which is equivalent to a M_w 6.2 event and slightly larger than the seismic moment estimates of the BATS and Harvard CMT solutions (M_w 6.1). Most aftershocks occurred on the northern portion of the rupture, suggesting that the coseismic slip possibly did not fully release the accumulated strain in this area during the main shock, thereby explaining the relatively small coseismic slip inferred in our model compared to that in the southern portion.

The coseismic fault geometry obtained in our study is similar to the result reported by Wu *et al*. (2006) where they chose the fault geometry of strike 18° and dip 77°W from the distribution of aftershocks. Because of the lack of strong motion stations near and to the north of the epicenter, Wu *et al*. (2006) were not able to observe the transition in the coseismic displacement pattern that we found in our study. The northern section exhibited predominantly left-lateral slip, while the southern segment exhibited a larger amount of oblique slip with a significant thrust component. Based on 59 GPS three-component displacement vectors (three times data in Wu *et al*., 2006) as well as 81 leveling vertical measurements, the transition zone of slip behaviors in our study was located further south, at 22°50′N, in comparison to that found by Wu *et al*. (2006).

The drastic change in slip behaviors on the Y fault leads to the aforementioned possibility of a coseismic E-W-trending right-lateral faulting. This fault would cut across the Y fault at the transition zone a little south of the hypocenter, which is also consistent with the focal mechanism of the main shock. The cluster of aftershocks that occurred around this possible fault also strengthens the speculation. If so, the E-W fault would mark the boundary of distinct coseismic displacements in the footwall of the Y fault between the north and south and also the discrepancy of slip distributions between the north and south portions. The E-W-trending strike-slip fault in the north-middle of Peinanshan massif has been argued in a geological context from a few pieces of evidence based on geomorphic signatures and

Table 5. The elevation differences and accumulative elevation changes of the six leveling routes during the 4 months prior to and 2 months after the 2006 Peinan earthquake. The columns include station names (from benchmark A to B), positions at "from" benchmark in latitude, longitude and elevations, elevation differences (dH), accumulative elevation changes (A_c_dH) and their standard deviations, respectively.

From	To	Latitude (°)	Longitude (°)	Elevation (m)	dH (mm)	A_c_dH (mm)
Route 1						
9190	S273	22.7649	121.0421	114.8	−15.5±1.6	48.0±5.0
S273	9189	22.7671	121.0547	97.2	−24.5±1.2	32.5±5.0
9189	8004	22.7726	121.0669	80.3	−24.6±1.2	8.0±4.7
8004	9188	22.7765	121.0781	62.7	−8.7±0.4	−16.6±4.5
9I88	8005	22.7760	121.0852	56.2	−7.0±0.6	−25.3±4.4
8005	8006	22.7752	121.0916	49.2	−10.2±1.0	−32.3±4.4
8006	S274	22.7793	121.0993	42.5	−12.8±0.3	−42.5±4.3
S274	9184	22.7804	121.1005	46.9	17.6±1.1	−55.3±4.2
9184	S266	22.7877	121.1073	45.4	9.0±1.5	−37.7±4.2
S266	GE04	22.7860	121.1200	34.1	−0.2±1.3	−28.7±4.0
GE04	S267	22.7920	121.1275	32.8	0.9±0.2	−28.9±3.8
S267	138R	22.7918	121.1294	34.9	0.1±0.5	−28.0±3.5
138R	S268	22.7932	121.1326	37.4	2.6±0.7	−27.9±3.5
S268	S269	22.7944	121.1374	37.9	−2.6±0.8	−25.4±3.5
S269	205R	22.7927	121.1456	36.6	11.1±2.3	−27.9±3.4
205R	8011	22.7818	121.1568	15.8	1.9±1.2	−16.8±3.3
8011	A087	22.7791	121.1663	7.5	2.7±1.3	−14.9±2.4
A087	8013	22.7902	121.1750	7.3	2.9±1.0	−12.2±2.1
8013	8014	22.7967	121.1860	28.2	1.4±1.0	−9.3±1.6
8014	GE11	22.8096	121.1875	14.7	−0.2±0.7	−8.0±1.3
GE11	A084	22.8136	121.1859	11.8	−1.6±0.3	−8.1±0.8
A084	8015	22.8175	121.1848	20.8	2.3±0.3	−9.8±0.4
8015		22.8230	121.1814	12.0		−7.5±0.3
Route 2						
T041	T042	22.8051	121.0512	230.7	−20.9±0.4	62.0±1.2
T042	T043	22.8057	121.0542	205.4	−8.2±0.6	41.1±1.2
T043	T044	22.8076	121.0599	174.5	−11.8±0.3	32.8±1.2
T044	T045	22.8081	121.0650	155.6	−8.1±0.1	1.1±1.0
T045	T046	22.8070	121.0699	138.2	−13.9±0.5	12.9±0.9
T046	T031	22.8050	121.0750	120.2	−15.0±0.5	−1.0±0.9
T031	T032	22.8020	121.0800	103.7	−5.3±0.3	−16.0±0.8
T032	T033	22.7993	121.0846	88.3	−18.2±0.5	−21.3±0.6
T033	TA10	22.7942	121.0894	73.0	−1.3±0.2	−39.5±0.5
TA10		22.7907	121.0918	66.1		−40.8±0.2
Route 3						
S206	S205	22.9158	121.0838	226.7	−3.0±0.3	−0.7±1.6
S205	S239	22.9097	121.0846	199.7	1.8±0.6	−3.5±1.6
S239	S203	22.9071	121.0933	203.2	4.0±0.6	−1.7±1.6
S203	S238	22.9060	121.1031	193.7	9.1±0.2	2.2±1.5
S238	S201	22.9059	121.1063	203.3	−1.0±0.1	11.3±1.4
S201	S200	22.9058	121.1087	201.9	−0.9±0.4	10.3±1.3
S200	S199	22.9055	121.1171	185.2	−2.2±0.9	10.2±1.3
S199	8051	22.9076	121.1277	163.8	−0.6±0.9	8.0±1.3
8051	S234	22.9122	121.1283	138.6	1.8±0.7	7.7±3.9
S234	S242	22.9088	121.1321	117.7	6.8±0.5	10.5±1.2
S242	S236	22.9085	121.1398	119.0	7.0±1.0	17.3±1.3
S236	S237	22.9039	121.1434	160.1	−1.4±0.7	23.2±1.6
S237	W048	22.8995	121.1414	163.4	2.8±1.2	22.6±1.7
W048		22.9031	121.1457	216.9		25.3±2.1

field observations (Barrier and Angelier, 1986; Lee *et al*., 1998). However, the dynamic coseismic rupturing on the E-W-trending fault needs further investigation, in particular, to be the subject of a detailed seismological study. It is also worthy to note that in our study, the dip-slip component is larger than left-lateral strike-slip component on the southern section, which is opposite to results reported by Wu *et al*. (2006).

Table 5. (continued).

From	To	Latitude (°)	Longitude (°)	Elevation (m)	dH (mm)	A_c dH (mm)
Route 4						
S207	S198	22.9416	121.1165	265.5	4.4±0.7	9.8±0.7
S198	S197	22.9405	121.1187	259.1	−3.8±0.7	13.6±0.7
S197	S196	22.9392	121.1201	258.3	2.0±0.7	9.2±1.5
S196	S195	22.9366	121.1245	233.5	2.1±1.1	10.7±1.4
S195	8050	22.9337	121.1278	224.5	−6.8±0.3	12.1±1.2
8050	9172	22.9269	121.1361	140.6	2.3±1.0	5.3±4.0
9172	S127	22.9336	121.1371	148.0	−7.4±0.6	6.9±1.0
S127	S128	22.9434	121.1444	159.6	−2.4±0.2	−1.0±1.2
S128	0308	22.9420	121.1491	151.7	−1.9±0.6	−3.5±1.2
0308	S194	22.9440	121.1528	150.7	12.9±1.1	−5.8±1.3
S194	S193	22.9447	121.1561	169.8	33.0±1.0	6.6±1.7
S193		22.9428	121.1608	195.4		38.8±2.0
Route 5						
S245	V108	22.9808	121.1292	230.0	0.1±1.3	2.3±0.0
V108	S246	22.9757	121.1491	188.5	−2.3±0.8	2.3±1.3
S246	V109	22.9758	121.1567	165.9	11.9±0.5	−0.2±1.5
V109	S247	22.9747	121.1663	165.0	9.9±0.1	11.7±1.7
S247	V110	22.9750	121.1688	217.5	11.2±0.4	21.6±1.7
V110	S248	22.9742	121.1749	312.5	0.5±1.4	27.4±1.8
S248		22.9773	121.1786	369.1		27.9±2.3
Route 6						
9184	9183	22.7877	121.1073	45.4	7.7±0.7	−37.7±4.7
9183	S260	22.7965	121.1924	69.1	20.7±0.5	−30.0±0.7
S260	9182	22.8026	121.0865	89.8	6.9±0.4	−9.3±0.9
9182	8059	22.8083	121.0848	100.6	8.5±0.9	−2.4±0.9
8059	TP1	22.8176	121.0814	119.9	1.5±0.8	6.2±1.3
TP1	9181	22.8230	121.0828	134.3	−1.7±1.1	7.7±1.5
9181	8058	22.8328	121.0858	156.2	0.1±0.1	6.0±1.9
8058	8057	22.8357	121.0858	161.1	2.8±0.8	6.1±1.9
8057	9180	22.8512	121.0843	200.9	1.7±0.6	8.9±2.1
9180	9179	22.8551	121.0842	207.3	−4.1±0.9	10.7±2.1
9179	8055	22.8658	121.0866	233.8	−0.0±0.9	6.5±2.3
8055	9178	22.8751	121.0911	231.5	−1.9±0.5	8.4±2.5
9178	T052	22.8823	121.0963	218.5	1.6±0.6	6.5±2.6
T052	9177	22.8909	121.0853	206.7	0.9±1.8	8.1±2.6
9177	T054	22.8954	121.0870	160.6	0.9±0.9	9.0±3.2
T054	9176	22.9012	121.0912	161.9	−1.0±0.2	9.9±3.3
9176	9175	22.9014	121.0920	166.8	4.7±0.9	8.9±3.3
9175	8052	22.8957	121.1145	129.1	3.3±0.9	13.6±3.5
8052	9174	22.8950	121.1276	121.1	−7.1±0.5	16.9±3.6
9174	8051	22.9018	121.1285	125.1	−2.1±1.4	9.8±3.6
8051	8050	22.9125	121.1281	138.6	−2.3±1.0	7.7±3.9
8050		22.9268	121.1361	140.6		5.3±4.0
Route 6-1						
9184	9183	22.7877	121.1073	45.4	7.7±0.7	−37.7±4.7
9183	S260	22.7965	121.1924	69.1	21.0±0.5	−30.0±0.7
S260	S275	22.8026	121.0865	89.8	−13.9±1.0	−9.0±0.8
S275	S276	22.7933	121.0835	83.3	−6.8±0.3	−23.0±1.2
S276	S272	22.7676	121.0784	80.1	38.3±0.9	−29.7±1.3
S272		22.7929	121.0689	118.0		8.5±1.6
Route 6-2						
9184	9183	22.7877	121.1073	45.4	7.7±0.7	−37.7±4.7
9183	S260	22.7965	121.1924	69.1	20.7±0.5	−30.0±0.7
S260	S261	22.8026	121.0865	89.8	−3.4±0.9	−9.3±0.9
S261	S262	22.8105	121.0896	191.4	1.3±1.0	−10.3±1.3
S262	S263	22.8171	121.0888	220.3	−0.3±0.5	−9.1±1.6
S263	TP01	22.8258	121.0921	265.8	19.8±1.5	−9.3±1.7
TP01	8059	22.8230	121.0828	134.3	−1.5±0.8	10.4±2.3
8059		22.8176	121.0814	119.9		8.9±2.4

7. Conclusions

Based on data from a dense geodetic network, including seven continuous GPS stations, 52 campaign-mode GPS sites, and six leveling routes, we estimated both the horizontal and vertical surface coseismic displacements associated with the 2006 M_w 6.1 Peinan earthquake. By integrating geodetic measurements with seismological information, we conclude that the Peinan earthquake resulted from a rupturing of a geologically suspected fault under the eastern margin of the Central Range. We also named this fault as the Y fault. We used an elastic half-space dislocation model and all available data in an inversion to determine the fault geometry and the coseismic slip distribution. The optimal modeled fault is a 25-km-long, 80° west-dipping plane at a depth between 0.5 and 20 km, indicating a buried fault. Our results show different slip behaviors between the epicenter area and the area to the south, as revealed by the coseismic surface deformation and the slip distribution on the causative Y fault. The inferred slip distribution on the Y fault showed a maximum coseismic slip of 0.33 m at a depth of 9–16 km, which is about 10 km south of the hypocenter. Fault slip is mainly left-lateral strike-slip on the northern portion near the hypocenter; however, it turns sharply into oblique left-lateral reverse slip on the southern portion. The total geodetic moment is 2.3×10^{18} Nt-m, which is equivalent to a M_w 6.2 event.

Acknowledgments. The authors would like to express their sincere gratitude to their colleagues in Geodetic Group at IESAS, also for their help doing the GPS field work and collecting continuous GPS data from the permanent stations. We are grateful to the generous provision of continuous GPS data by the CWB as well as precise ephemeredes of GPS satellites by the IGS community. This research was supported by the Taiwan Earthquake Research Center (TEC) funded through National Science Council (NSC) with grant number NSC95-2119-M-001-055 and is a contribution of Institute of Earth Sciences, Academia Sinica, IESAS1311. The TEC contribution number for this article is 00047.

References

Angelier, J., H. T. Chu, and J. C. Lee, Shear concentration in a collision zone: kinematics of the active Chihshang Fault, Longitudinal Valley, eastern Taiwan, *Tectonophys.*, **274**, 117–144, 1997.

Barrier, E. and J. Angelier, Active collision in eastern Taiwan: the Coastal Range, *Tectonophys.*, **274**, 117–143, 1986.

Barrier, E., J. Angelier, H. T. Chu, and L. S. Teng, Tectonic analysis of compressional in an active collision zone: the deformation of Pinanshan Conglomerates, eartern Taiwan, *Proc. Geol. Soc. China*, **25**, 123–138, 1982.

Biq, C. C., The eastern Taiwan rift, *Petrol. Geol. Taiwan*, **4**, 93–106, 1965.

Bock, Y., R. M. Nikolaidis, P. J. de Jonge, and M. Bevis, Instantaneous geodetic positioning at medium distances with the Global Positioning System, *J. Geophys. Res.*, **105**, 28,223–28,253, 2000.

Chen, H. Y., L. C. Kuo, W. S. Chuang, and S. B. Yu, Using Quasi Ionosphere-Free post-processing algorithm on the medium-range kinematic high accuracy GPS relative positioning, *Wuhan Univ. J. Nat. Sci.*, **8**, 2B, 610–618, 2003.

Chen, H. Y., Y. R. Chuang, S. B. Yu, and H. Y. Hu, GPS measurements of near-fault crustal deformation in the south Longitudinal Valley southeastern Taiwan, *2004 Int. Symp. on GPS/GNSS*, Sydney, Australia, 6–8 December, Paper No. 27, 2004.

Ho, C. S., A synthesis of the geologic evolution of Taiwan, *Tectonophys.*, **125**, 1–16, 1986.

Hsu, T. L., Recent faulting in the Longitudinal Valley of eastern Taiwan, *Proc. Geol. Soc. China Mem.*, **1**, 95–102, 1962.

Hu, J. C., J. Angelier, C. Homberg, and J. C. Lee, Three-dimensional modeling of the behavior of the oblique convergent boundary of southeast Taiwan: friction and strain partitioning, *Tectonophys.*, **333**, 261–276, 2001.

Hugentobler, U., S. Schaer, and P. Fridez, *Bernese GPS software Version 4.2*, 515 pp., Astro. Inst., Univ. of Berne, Berne, Switzerland, 2001.

Lee, J. C. and J. Angelier, Localisation des déformations actives et traitements des données géodésiques: l'example de la faille de la Vallée Longitudinal, *Taïwan. Bull. Soc. Geol. France*, t. 164, n° 4, 533–540, 1993.

Lee, J. C., J. Angelier, H. T. Chu, S. B. Yu, and J. C. Hu, Plate-boundary strain partitioning along the sinistral collision suture of the Philippine and Eurasian plates: Analysis of geodetic data and geological observation in southeastern Taiwan, *Tectonics*, **17**(6), 859–871, 1998.

Lee, J. C., J. Angelier, H. T. Chu, J. C. Hu, F. S. Jeng, and R. J. Rau, Active Fault Creep Variations at Chihshang, Taiwan, Revealed by Creepmeter Monitoring, 1998–2001, *J. Geophys. Res.*, **108**(B11), 2528, doi:10.10129/2003JB002394, 2003.

Lu, C. Y. and J. Malavieille, Oblique convergence, indentation and rotation tectonic in the Taiwan mountain belt: insights from experimental modeling, *Earth Planet. Sci. Lett.*, **121**, 477–494, 1994.

Matthews, M. and P. Segall, Statistical inversion of crustal deformation data and estimation of the depth distribution of slip in the 1906 earthquake, *J. Geophys. Res.*, **98**, 12153–12163, 1993.

Menke, W., *Geophysical data analysis: discrete inverse theory*, 260 pp., Academic Press, 1984.

Okada, Y., Surface deformation due to shear and tensile faults in a half-space, *Bull. Seismol. Soc. Am.*, **75**, 1135–1154, 1985.

Shyu, J. B. H., L. H. Chung, Y. G. Chen, J. C. Lee, and K. Sieh, Re-evaluation the surface ruptures of the November 1951 earthquake series in eastern Taiwan, and its neotectonic implications, *J. Asian Earth Sci.*, **31**, 317–331, doi:10.1016/j.jseaes.2006.07.018, 2007.

Shyu, J. B. H., K. Sieh, Y. G. Chen, R. Y. Chuang, Y. Wang, and L. H. Chung, Geomorphology of the southernmost Longitudinal Valley fault: Implications for evolution of the active suture of eastern Taiwan, *Tectonics*, **27**, tc1019, doi:10.1029/2006TC002060, 2008

Wu, Y. M., Y. G. Chen, C. H. Chang, L. H. Chung, T. L. Teng, F. T. Wu, and C. F. Wu, Seismogenic structure framework in a tectonic suture zone: with new constraints from 2006 M_w 6.1 Taitung earthquake, *Geophys. Res. Lett.*, **33**(22), L22305, 2006.

Yu, S. B. and C. C. Liu, Fault creep on the central segment of the Longitudinal Valley fault, eastern Taiwan, *Proc. Geol. Soc. China*, **32**(3), 209–231, 1989.

Yu, S. B. and L. C. Kuo, Present-day crustal motion along the Longitudinal Valley fault, eastern Taiwan, *Tectonophys.*, **333**, 199–217, 2001.

Yu, S. B., G. K. Yu, L. C. Kuo, and C. Lee, Crustal deformation in the southern Longitudinal Valley area, eastern Taiwan, *J. Geol. Soc. China*, **35**(3), 219–230, 1992.

Yu, S. B., Y. J. Hsu, L. C. Kuo, H. Y. Chen, and C. C. Liu, GPS measurement of postseismic deformation following the 1999 Chi-Chi, Taiwan, earthquake, *J. Geophys. Res.*, **108**(B11), 2520, doi:10.1029/2003JB002396, 2003.

H.-Y. Chen (e-mail: chenhy@earth.sinica.edu.tw), Y.-J. Hsu, J.-C. Lee, S.-B. Yu, L.-C. Kuo, Y.-L. Jiang, C.-C. Liu, and C.-S. Tsai